Modeling spatially dependent kinetics of helium desorption in BCC iron following He ion implantation

Donghua Xu *, Brian D. Wirth

Department of Nuclear Engineering, University of California, Berkeley, CA 94720-1730, USA

ARTICLE INFO

ABSTRACT

One of the most important tasks in fusion materials research is to study the effect of helium on the microstructure and mechanical property evolution of structural materials. Thermal helium desorption spectrometry (THDS), through measuring the outward He surface flux as a function of temperature (or time), provides indirect information about the kinetics and energetics of helium transport and trapping/detrapping which is important for developing a predictive assessment for the life performance of fusion reactors. Nevertheless, THDS data interpretation is not straightforward, particularly when a broad temperature regime and a high He concentration are concerned. Here we present results from a spatially-dependent rate theory modeling framework in coordination with our previous THDS experiments on single crystal iron implanted with ^{4}He$^+$ ions at 5 or 10 keV to fluences of 10^{18} or 10^{19} He/m^2. The model incorporates both temporally and spatially dependent diffusion, trapping, and detrapping (emission) kinetics for both implantation process and post-implantation thermal annealing. Possible desorption sequences/mechanisms are discussed.

© 2010 Elsevier B.V. All rights reserved.

1. Introduction

As a result of direct helium implantation and (n, α) transmutation reactions, a high concentration of helium will be accumulated in the structural materials in future fusion reactors [1–3]. Because of very low solubility, helium resides in the materials primarily in the state of being trapped by atomic defects such as vacancies, interstitials and their clusters, as well as extended defects such as dislocations, grain boundaries and cavities or precipitate interfaces. Under certain circumstances, the small He-containing complexes can reach a critical state and trigger the nucleation and growth of large He bubbles, and at larger sizes the He bubbles can convert to unstably growing voids [1–8]. The formation of He bubbles in the grains or along the grain boundaries leads to significant radiation hardening or degradation in creep rupture behavior, and can further result in premature failure of the materials under relatively low stress. Evidently, studying how He migrates (diffusion), and interacts (trapping/detrapping) with atomistic/nanoscopic/microscopic defects is crucial for the understanding and ultimate control of He effects on structural materials.

Research on the role of helium (as well as other inert gases) in radiation damage was started in the 1970s (see, e.g., Refs. [4,7,8]) with concerns mainly focused on fission relevant conditions. A theoretical framework was then founded for analyzing the defect cluster dynamics with or without inert gases. In recent years, helium has received increased attention as a result of the resurgent interest in fusion energy. A surging number of studies related to He in structural materials have been and are being published in the literature. In BCC iron and ferritic alloys, specifically, the kinetics, energetics and thermal stabilities of He and small He-containing clusters, and He interactions with dislocations and grain boundaries have been studied computationally using *ab* initio and molecular statics/dynamics approaches (e.g., [9–14]), while experiments using optical or electron microscopy (e.g., [15]), nuclear reaction depth profiling [16], positron annihilation spectroscopy (lifetime and coincidence Doppler broadening) [17], thermal desorption (e.g., [18,19]) and other techniques have been conducted to analyze He behavior and the coupled He and defect evolution. However, the overall picture of He in BCC iron or ferritic alloys remains incomplete and not yet self-consistent. On one hand, there are still significant unresolved questions such as the energetics of large He–V clusters. On the other hand, apparent discrepancies still exist in the literature regarding some fundamental subjects, such as the binding energy of a HeV cluster.

With an aim to validate the existing knowledge in this area and to possibly provide additional information, we have recently conducted thermal desorption experiments on He-implanted iron. Both poly-crystal and single crystal specimens were examined and the experimental results were reported in an earlier publication [20]. Our data for the single crystal specimens, probably the first set for iron, is expected to better serve the validation purpose because of reduced complexity associated with grain boundaries.

---

* Corresponding author.
  E-mail addresses: xudh@nuc.berkeley.edu (D.H. Xu), bdwirth@nuc.berkeley.edu (B.D. Wirth).

However, even for the single crystal specimens, complete interpretation of the desorption data is not straightforward and requires detailed modeling which takes into account the migration, trapping and detrapping (emission) kinetics of defects and/or defect clusters. Due to the highly localized production of defects and stopping of He ions under our implantation conditions (the experimental parameters will be briefly reviewed below; for more details, refer to Ref. [20]), spatial dependence has to be included in the model, which has been mostly neglected in conventional rate theory modeling. Further, the thermal annealing to drive the He desorption was performed at a constant heating rate with the temperature running across several hundreds of degrees. Within such a broad temperature range, the diffusivities of point defects and the trapping/emission interaction rate constants vary by several orders of magnitude. Both the spatial dependence and the broad temperature regime significantly increase the difficulty of modeling such experiments.

In an earlier attempt [21] of modeling these experiments, we obtained first results for the specimens implanted to a lower fluence (10^{18} He/m^2), while the desorption of the higher fluence (10^{19} He/m^2) specimens was not able to be modeled due to the high requirement for both memory and CPU time which went beyond the capability of our spatially-dependent cluster dynamics code and available hardware. More recently we have developed a new code with heavily reduced memory usage and implemented Open-MP parallelism to simultaneously utilize multiple processors for compute-intensive iterations and function/array/matrix/tensor evaluations/operations, and for solving involved large sparse linear algebraic systems. The new code can handle large systems of 20 million or more ordinary differential equations with decent efficiency. Moreover, an adaptive phase-cut approach (to be reported elsewhere) has been developed to eliminate from the calculations irrelevant compositions in the He–V/I phase space (to be defined later), which further enhances the power of the current code. In this present paper we focus on the new results for the higher fluence specimens as well as for the lower fluence specimens with newly optimized model parameters.

2. Summary of helium desorption experiments

The desorption experiments were performed on high purity (~99.94%) single crystal iron, following room temperature implantation with ^{4}He$^+$ ions at energies of 5 or 10 keV to fluences of 10^{18} or 10^{19} He/m^2. The nominal implantation flux was ~1 × 10^{15} He/ m^2/s. Constant rate (1 K/s) heating ramps were used to thermally desorb He from the specimens. As can be seen from Fig. 1 (gray dots), at all four combinations of implantation energies and fluencies, two well separated major desorption groups are clearly observed within the BCC temperature range (up to 912 °C), Group I below ~300 °C, and Group II from ~550 °C to 912 °C. Further, increasing implantation fluence from 10^{18} to 10^{19} He/m^2 greatly increases the fraction of retained He that does not desorb until ~1200 °C.

3. Model setup and initial parameterization

As illustrated in Fig. 2, we treat the current modeling as a multidimensional problem, with two dimensions (one for the number of He, the other for the number of vacancy, if positive, or interstitial, if negative, in a defect/cluster) in the phase space, one dimension (depth along implantation direction) in the geometric space, and one dimension in time. The direct task of the modeling is to solve for the time dependent concentration of each defect/cluster as defined by an arbitrary He number and an arbitrary vacancy/interstitial number in the phase space at different depth during both the implantation process and the post-implantation thermal annealing
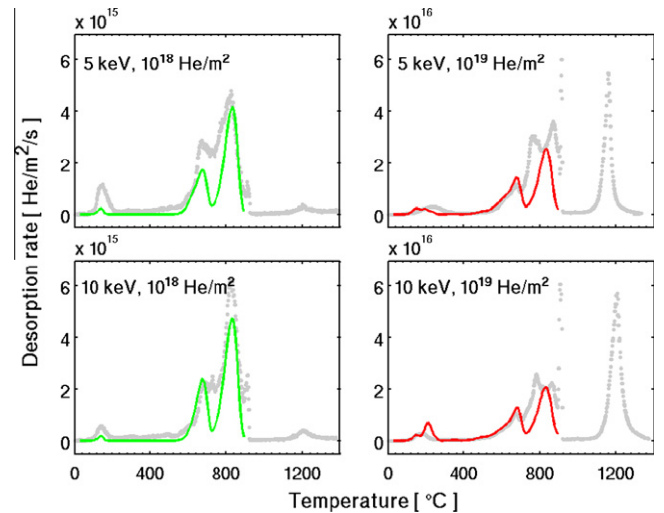

Fig. 1. Experimental (gray dots) and predicted (solid lines) He desorption spectra in single crystal iron implanted with ^{4}He$^+$ ions, for different He implantation energy and fluence.

(1 K/s ramp). Note that currently we do not consider the clustering of He with interstitials, which is similar to other modeling studies (e.g. [14]).

One ordinary differential equation (ODE) is established for each defect/cluster at each depth. The structure of the ODE varies according to the type of the defect/cluster. If the defect/cluster is immobile, the equation is structured as,

$$\frac{\partial C_{immob}}{\partial t} = GRT + GRE - ART - ARE, \tag{1}$$

where *GR* refers to summed generation (formation) rates, *AR* refers to summed annihilation (consumption) rates, *T* refers to generation or annihilation by trapping events, and *E* refers to generation or annihilation by emission events. For example, a He$_3$V$_5$ (immobile) can be generated by the following trapping events: a He$_2$V$_5$ (immobile) trapping a nearby He interstitial (mobile), a He$_3$V$_4$ (immobile) trapping a nearby vacancy (mobile), a He$_3$V$_6$ trapping a nearby self-interstitial-atom (SIA, mobile), or, a He$_3$V$_7$ trapping a nearby di-SIA (mobile). On the other hand, the He$_3$V$_5$ cluster can transform to another cluster and thus annihilate (consume) itself by trapping the mobile species around it. Clearly, the number of trapping events that could generate or annihilate a given cluster depends on the number of mobile species. In the present model, we consider only point defects (He, V, I) and di-SIA (I$_2$) as mobile, consistent with other works [14]. However, future model calculations will consider the effect of mobile interstitial clusters, as well as the mobility of small He–vacancy clusters.

Furthermore, a He$_3$V$_5$ can also be generated by a He$_4$V$_5$ emitting a He interstitial, a He$_3$V$_6$ emitting a vacancy, or, a He$_3$V$_4$ emitting an SIA, and similarly, a He$_3$V$_5$ can also lose its identity by emitting a He, a vacancy or an SIA. Note that for the emission, we only consider the release of a single point defect at a time and neglect the possibility of the release of a di-SIA by any cluster. For the trapping/emission rate constants we use the same formulism as in Ref. [22] except that for the trapping radius we use a more conventional definition (e.g., [4,7,23]) which does not carry modifications made in [22] for the interstitial/vacancy bias and interstitial-vacancy recombination distance. The bias factor and the recombination distance are separately applied to the relevant interactions in this work. Note that this treatment of trapping radius is different from our initial calculations reported in [21].

Different from Eq. (1), the equation for di-SIA I$_2$, which is mobile, is structured as
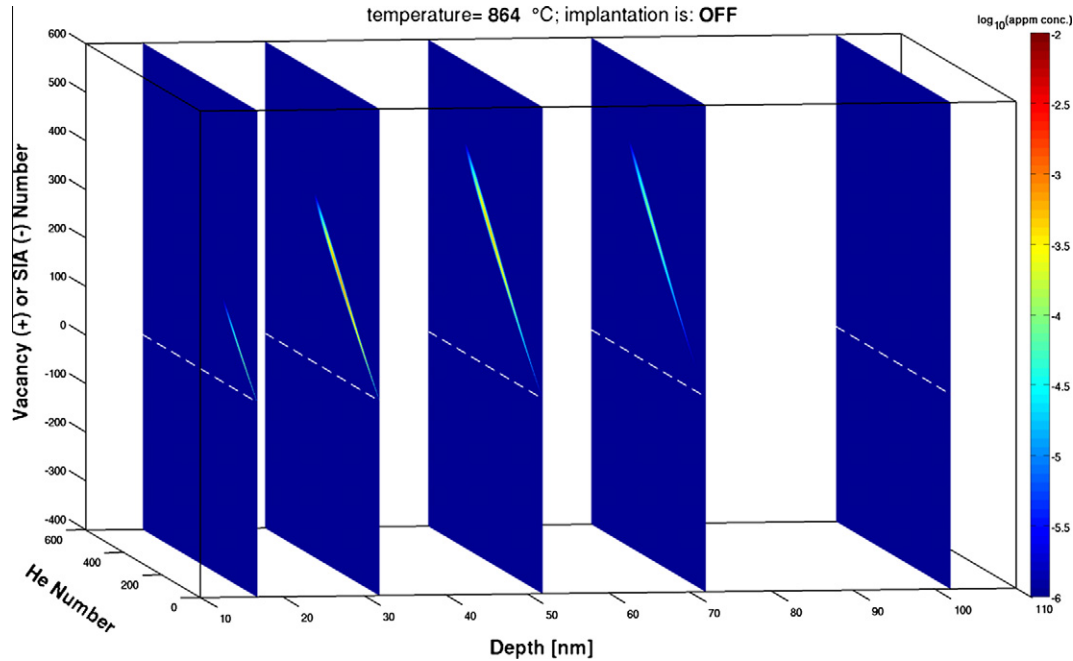
Fig. 2. A snapshot from the model prediction showing the He–vacancy–interstitial cluster phase space distribution as a function of spatial positions (depth) at 864 °C for a specimen implanted with 10 keV He to 10^{19} He/m². The dotted lines correspond to zero-vacancy and are included to guide the eye. Note that many more spatial points are included in the model calculation, although only five are displayed here.

$$\frac{\partial C_{I_2}}{\partial t} = D_{I_2}\frac{\partial^2 C_{I_2}}{\partial x^2} + GRT + GRE - ART - ARE - 1.15$$
$$\times \rho_{disl} \times D_{I_2} \times C_{I_2}, \qquad (2)$$

where the first term on the right hand side (RHS) is added to account for the diffusion of I_2 across neighboring spatial positions (x), and the last term is for the loss of di-interstitials to dislocation sinks with a bias factor of 1.15 (note, that the calculation results are not very sensitive to the bias; a value of 1.1 makes little difference).

The equation for single interstitial He is structured as

$$\frac{\partial C_{He}}{\partial t} = \phi \times P_{He}(x) + D_{He}\frac{\partial^2 C_{He}}{\partial x^2} + GRT + GRE - ART - ARE, \qquad (3)$$

where the first term on RHS is inserted to account for the generation of He by implantation, with ϕ being the implantation flux and $P_{He}(x)$ being spatially dependent He-stopping probability function predicted by SRIM/TRIM [24]. Note that although interstitial He is a point defect, it can still be generated by trapping reactions $HeV + I = He$ and $HeV_2 + I_2 = He$, and can also lose its identity by emitting (producing) an SIA, i.e., $He = HeV + I$. At present, we do not consider He loss to sinks, since it cannot lose its identity, nor do we consider its binding with, dissociation from or diffusion along, dislocation lines in the present model due to the uncertainty in the dislocation structures/types which could affect how strongly the dislocations interact with He according to some atomistic calculations [13].

The equations for single SIA and V are structured as, respectively,

$$\frac{\partial C_I}{\partial t} = \phi \times P_{FP}(x) + D_I\frac{\partial^2 C_I}{\partial x^2} + GRT + GRE - ART - 1.15$$
$$\times \rho_{disl} \times D_I \times C_I, \qquad (4)$$

and,

$$\frac{\partial C_V}{\partial t} = \phi \times P_{FP}(x) + D_V\frac{\partial^2 C_V}{\partial x^2} + GRT + GRE - ART - 1 \times \rho_{disl}$$
$$\times D_V \times (C_V - C_V^{eq.}), \qquad (5)$$

where $P_{FP}(x)$ is the SRIM/TRIM predicted generation probability function for Frenkel pairs, and $C_V^{eq.}$ is the thermal equilibrium concentration of single vacancies. Note that single SIA and V can be generated by trapping reactions $I_2 + V = I$, $V_2 + I = V$ and $V_3 + I_2 = V$, but they cannot undergo any type of emission and thus the *ARE* term disappears in Eqs. (4), (5).

For all the mobile species (Eqs. (2)–(5)), to calculate the second derivative of concentration over x, we use the common finite difference formulism, i.e.,

$$\left.\frac{\partial^2 C}{\partial x^2}\right|_{x_i} = \frac{\frac{C_{x_{i+1}} - C_{x_i}}{x_{i+1} - x_i} - \frac{C_{x_i} - C_{x_{i-1}}}{x_i - x_{i-1}}}{\frac{x_{i+1} - x_{i-1}}{2}}, \qquad (6)$$

at all interior spatial grids x_2 through x_{N-1} where N is the total number of spatial grids. Meanwhile, a Dirichlet boundary condition with all defect concentrations equal to zero is applied at x_1 and x_N, i.e., both surfaces are treated as perfect (black) sinks for all the defects. A typical magnitude of the dislocation density, 10^{14}/m², has been adopted in all the calculations while two other values, namely, 10^{13}/m² and 5×10^{14}/m², have also been inspected in a 10 keV and 10^{19} He/m² calculation which revealed no significant difference.

As mentioned in [21], we have used migration energies obtained from *ab initio* calculations [14], i.e., 0.42, 0.34 and 0.06 eV for I_2, I and He, respectively, while keeping the vacancy migration energy ($E_{m,V}$) as an optimization parameter. The binding energies of I_m and V_n clusters are extrapolated according to a 2/3 power law [25] from the *ab initio* data for small clusters, and the binding energies of $He_mV_n(m \neq 0)$ clusters are obtained through thermodynamics using the elastic relaxation model and the equation of state of He proposed by Trinkaus [7]. More details about the thermodynamic analysis and the obtained binding energies can be found in [21]. As discussed in the next Section, the binding energies of certain small He–V clusters need to be optimized to obtain reasonable agreement between the model and the experimental results.

4. Results and discussion

Previously in Ref. [21], we reported that the initial parameterization with $E_{m,V}$ = 0.9 eV and the binding energies directly from the extrapolation of the *ab initio* results (for I_m and V_n) and from thermodynamic calculations (for $He_m V_n$ (m > 0)) cannot reproduce the desorption spectra satisfactorily, particularly the low-T peak below 300 °C. However, by comparing the cluster distribution (as illustrated in Fig. 2) at different temperatures, some important clusters, particularly He_2V, He_3V_2, HeV, are able to be associated with the major peaks predicted by the model. Therefore, we have attempted to perform a parameter optimization, which is aimed at improving the agreement between the model and the experiments, and focused on tuning the binding energies of these critical clusters in addition to the vacancy migration energy.

The solid lines in Fig. 1 represent the modeled desorption spectra with the best overall agreement with the experiments (gray dots) obtained so far using a single set of optimized parameters: $E_{m,V}$ = 0.8 eV, $E_{bHe,HeV}$ = 3.2 eV (=$E_{bV,HeV}$), $E_{bHe,He2V}$ = 1.12 eV, $E_{b\ He,He3V2}$ = 2.45 eV, $E_{bHe,He4V2}$ = 1.18 eV, $E_{b\ He,He5V3}$ = 2.17 eV, where $E_{bHe,HemVn}$ is the binding energy of He with the $He_m V_n$ cluster as defined by the formation energy difference on the two sides of the reaction $He + He_{m-1}V_n \leftrightarrow He_m V_n$ (note that $E_{bV,HemVn}$ and $E_{bI,HemVn}$ in this work are also defined the same way). As can be seen in Fig. 1, quite similar to the experimental observations, the model predicts two well separated major desorption groups within the BCC temperature range, one below 300 °C, and the other above 550 °C. Moreover, the main peak positions are also reproduced fairly well by the model. On the other hand, the model requires further improvement or optimization to better reproduce the intensities of the desorption peaks as well as the splitting of the strongest peak (around 800 °C) within the BCC range for the two higher fluence (10^{19} He/m^2) specimens.

Larger values of the vacancy migration energy than the value of 0.67 eV predicted by *ab initio* [11] have also been reported in other computational studies that attempted to reproduce experimental desorption data (e.g., Ref. [14]). A typical explanation for this discrepancy is the inhibition of vacancy mobility by impurities, particularly carbon in iron. This explanation seems to be supported by a recent rate theory modeling work [26] where the explicit inclusion of a few small carbon-containing clusters $He_n V_m C_p$ (n, m, p = 0, 1, 2) along with *ab initio* vacancy migration energy is shown to produce

similar agreement with experiments to that obtained by an effective but larger vacancy migration energy without considering carbon. While it is likely that carbon can also explain the 0.8 eV vacancy migration energy in the present study, further experimental and computational investigations are required to verify this.

Table 1 compares the He-, V-, I-binding energies for small $He_m V_n$ (m, n = 1–5) clusters predicted by *ab initio* [14], molecular dynamics [9] and thermodynamic calculations [21], including the values (italised in the table) optimized in this work for the aforementioned five clusters. It can be seen from Table 1 that the optimized values in this study are closer to the thermodynamic predictions than to *ab initio* or MD calculations. The fact that thermodynamic predictions do need to be modified for the small clusters is not surprising since thermodynamics is not expected to be applicable to very small clusters. On the other hand, the clear disagreement among *ab initio*, MD, and thermodynamic calculations on the energetics of small clusters, and the correct way to extrapolate the *ab initio* or MD data to larger $He_m V_n$ clusters are in fact still open questions. Here we emphasize that in order to reliably validate the energetics of $He_m V_n$ clusters it is important to examine a wide temperature regime such as that in the present study which covers from room temperature up to 912 °C, the BCC to FCC phase transition temperature in Fe.

While the small clusters listed above with optimized binding energies are important species to accurately model the desorption spectra, they are not the sole players. In fact, helium release is intimately coupled to the overall cluster evolution dynamics and each desorption group involves a collective action of a distribution of cluster sizes. This is demonstrated in Figs. 3 and 4 where the temperature-evolving distributions of He–V clusters in the phase space at a selected depth of 37 nm are presented for the lower (10^{18} He/m^2) and the higher fluence (10^{19} He/m^2) specimens implanted with 10 keV He ions, respectively. Note that the cluster distributions for the specimens implanted with 5 keV He (not shown) are very similar to those presented for 10 keV in Figs. 3 and 4.

As shown in Fig. 3 for the lower fluence implantation, at 100 °C (representing a state after implantation and room temperature relaxation), the He–V clusters are rather small, with most clusters containing less than 10 He and less than 10 V, and the composition distribution is rather diffuse in both He and V directions. However, along the He direction it is confined by a boundary corresponding to a He/V ratio a bit larger than 2.5. The clusters with He/V ratio

Table 1
Comparison of the binding energies for small $He_m V_n$ (m, n = 1–5) clusters predicted by *ab initio* (14) (indicated by column heading 'A'), molecular dynamics (9) (column heading 'M') and thermodynamic calculations (21) (column heading 'T'). Italised are the values optimized in this work based on the thermodynamic data.

| | | He$_1$ | | | He$_2$ | | | He$_3$ | | | He$_4$ | | | He$_5$ | | |
		A	M	T	A	M	T	A	M	T	A	M	T	A	M	T
E_{bHe}	V$_1$	2.3	3.7	3.39 *3.2**	1.84	2.19	1.72 *1.12**	1.83	2.09	0.16	1.91	2.19	−1.16	n/a	1.99	−2.31
	V$_2$	2.85	3.71	3.75	2.75	3.8	3.17	2.07	2.81	2.29 *2.45**	2.36	2.48	1.43 *1.18**	n/a	2.52	0.65
	V$_3$	3.3	4.34	3.82	2.96	4.01	3.56	2.91	4.09	3.09	2.57	3.1	2.51	n/a	3.11	1.92 *2.1**
	V$_4$	3.84	4.72	3.85	3.12	4.23	3.71	3.16	4.2	3.44	3.05	4.23	3.06	n/a	3.13	2.62
	V$_5$	n/a	4.92	3.87	n/a	4.43	3.77	n/a	4.3	3.6	n/a	4.3	3.35	n/a	4.32	3.04
E_{bV}	V$_1$	2.3	3.7	3.39 *3.2**	3.71	5.13	10.1	4.59	5.82	18.94	5.52	6.55	29.54	n/a	5.8	41.71
	V$_2$	0.78	0.19	0.57	1.61	1.8	2.01	1.85	2.52	4.14	2.3	2.81	6.73	n/a	3.33	9.69
	V$_3$	0.83	0.97	0.5	1.04	1.18	0.9	1.8	2.47	1.7	2.03	3.09	2.77	n/a	3.68	4.05
	V$_4$	1.16	1.01	0.59	1.32	1.23	0.74	1.57	1.33	1.09	1.97	2.46	1.64	n/a	2.48	2.34
	V$_5$	n/a	0.82	0.68	n/a	1.02	0.74	n/a	1.13	0.91	n/a	1.2	1.21	n/a	2.38	1.63
E_{bI}	V$_1$	n/a	6.39	5.26	n/a	4.78	3.81	n/a	4.07	1.68	n/a	3.78	−0.91	n/a	3.25	−3.87
	V$_2$	n/a	5.61	5.32	n/a	5.4	4.92	n/a	4.12	4.13	n/a	3.5	3.05	n/a	2.9	1.77
	V$_3$	n/a	5.57	5.23	n/a	5.35	5.09	n/a	5.25	4.74	n/a	4.12	4.19	n/a	4.1	3.48
	V$_4$	n/a	5.76	5.15	n/a	5.56	5.08	n/a	5.45	4.91	n/a	5.38	4.61	n/a	4.2	4.2
	V$_5$	n/a	5.49	5.08	n/a	5.36	5.04	n/a	5.24	4.95	n/a	5.14	4.78	n/a	5.11	4.52

larger than this boundary value are essentially not formed because their binding energies with He or SIA are either very small positive or even negative within our thermodynamic model [21]. As the temperature increases to 350 °C, the He_2V cluster concentration is significantly reduced as the relatively low binding energy He is emitted (de-trapped). But at the same time, other clusters also experience significant evolution. Those with relatively low He/V ratios (above the diagonal in Fig. 3) become unstable with respect to V-binding and thus emit vacancies, and meanwhile, those with relatively high He/V ratios (below the diagonal, around the initial phase boundary mentioned above) become unstable with respect to He-binding and emit He. The He atoms de-trapped from the He_2V and other clusters partly diffuse to the surface and desorb, and partly re-trap with other clusters at the same depth or at a different depth during their diffusional migration. One interesting, but perhaps confusing phenomenon predicted by the model is that clusters above the He/V diagonal ratio appear to evolve towards even higher vacancy numbers (i.e., even lower He/V ratio) despite their weak binding with vacancies. This is because the V-binding energy of the He–V clusters, for a fixed He number, first decreases and then increases as the V-number increases. Therefore, vacancy emission first starts from the clusters with smaller or intermediate V-numbers and correspondingly, the clusters with larger V-numbers can initially capture more vacancies (from the smaller clus-

ters) but later emit vacancies as the annealing temperature continues to increase. This can be regarded as a vacancy-dominated Ostwald ripening process which is continuously damped because the de-trapped vacancies are constantly removed through annihilation at the microstructural sinks, including the free surfaces, dislocation lines and interstitial loops as the temperature rises. By ~550 °C (not shown in Fig. 3) this process is essentially complete, leaving a distribution of small clusters whose compositions are roughly along the He/V diagonal ratio of approximately 1 in the He–V cluster phase space. After this, these clusters (including He_3V_2) start to shrink along the diagonal, releasing both He and V. By 750 °C, as shown in Fig. 3, the remaining He dominantly exists in the form of a HeV cluster, which then dissociates as the temperature ramps towards 912 °C.

The higher fluence specimens, as shown in Fig. 4, follow quite a different evolution path. At 100 °C (or after the implantation), the cluster distribution, although similarly diffuse as in the low fluence specimens, is preferentially elongated along the He direction. Therefore, the concentrations of clusters with small He/V ratios (above the diagonal) are one to two orders of magnitude lower compared with the lower fluence (10^{18} He/m²). As a result, the initial low temperature evolution starting from ~100 °C does not involve vacancy-dominated Ostwald ripening, and the diffuse cluster distribution rapidly evolves into a line in the phase space with a
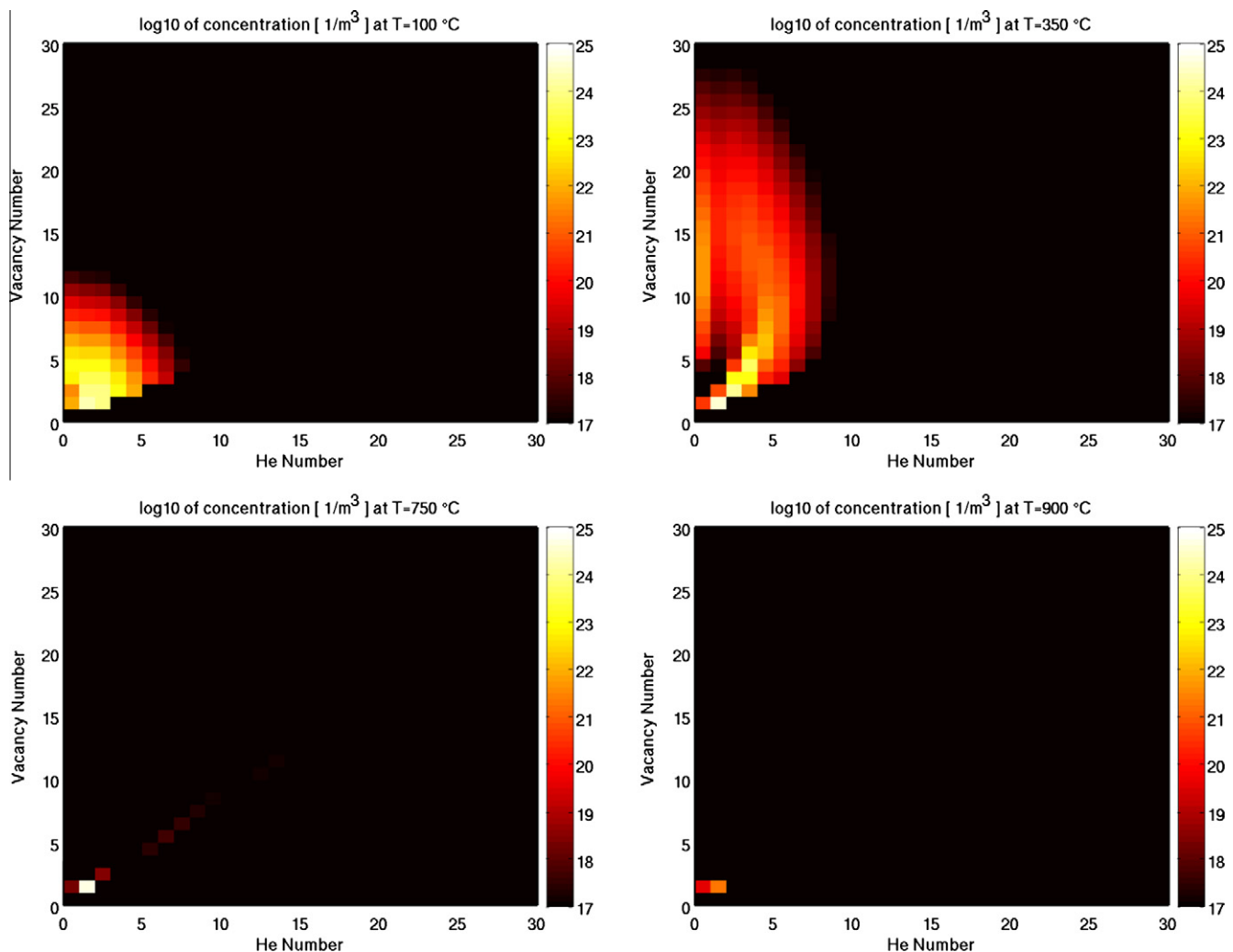

Fig. 3. Vacancy–He cluster phase space snapshots showing the cluster distribution evolution during the thermal annealing (at 1 K/s heating rate) at a depth of 37 nm for the specimen implanted with 10 keV He to the fluence of 10^{18} He/m². The depth of 37 nm is about midway between the peak Frenkel pair production depth and the most probable stopping position of He ions during implantation.
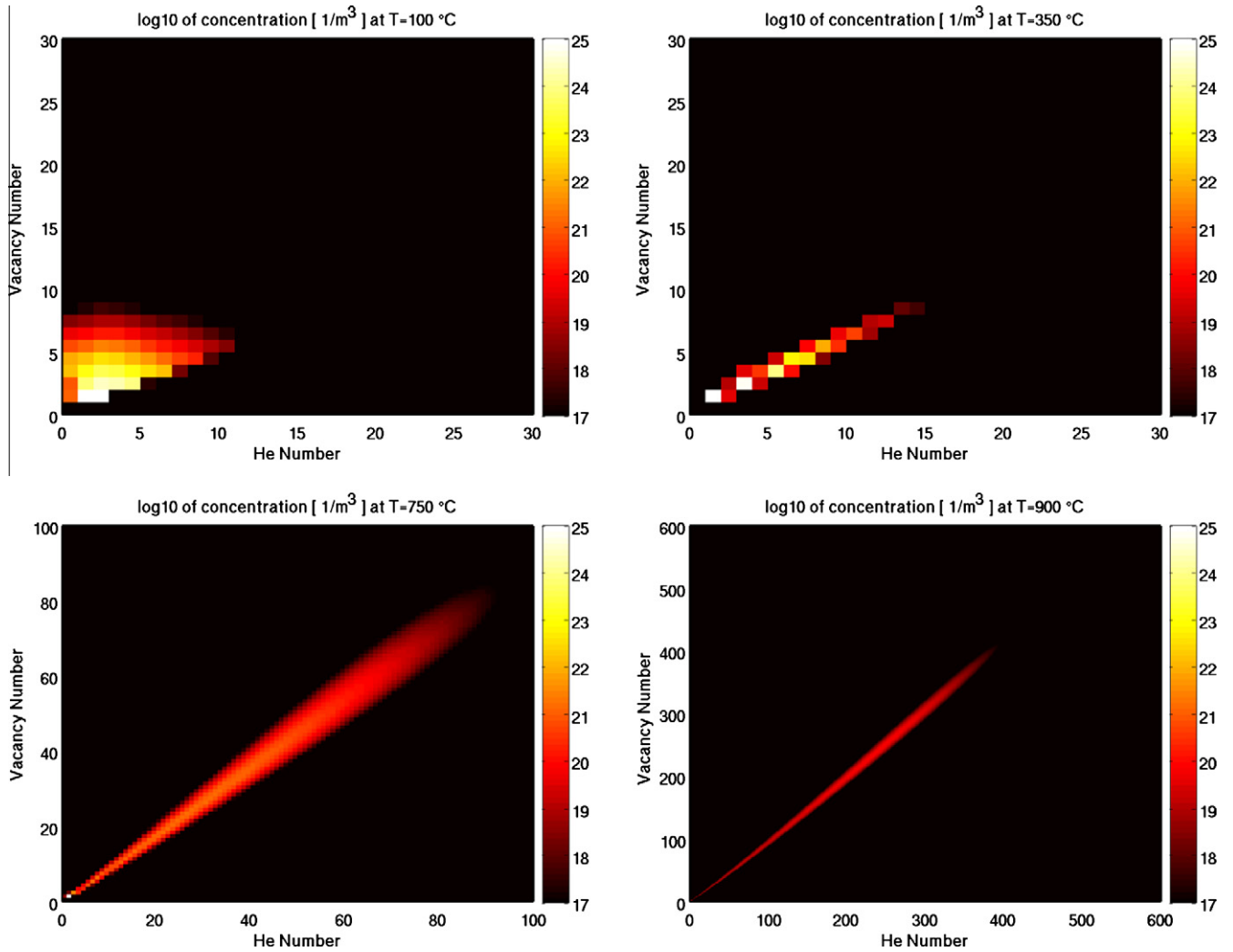
Fig. 4. Vacancy–He cluster phase space snapshots showing the cluster distribution evolution during the thermal annealing (at 1 K/s heating rate) at a depth of 37 nm for the specimen implanted with 10 keV He to the fluence of 10^{19} He/m^2. The depth of 37 nm is about midway between the peak Frenkel pair production depth and the most probable stopping position of He ions during implantation.

He/V ratio of ~1.6 by 350 °C. Next, as the temperature continues to rise, the line shrinks due to the emission of both He and V, while slowly changing the slope towards smaller He/V ratios. By ~600 °C (not shown in Fig. 4), the He/V ratio becomes close to 1, and the He$_3$V$_2$ cluster, as well as a few others such as He$_4$V$_3$ and He$_5$V$_4$, all begin to dissociate, releasing a large number of He and V. The increase in both He and V concentrations in the matrix leads to the formation of larger He–V clusters on the upper half of the He/V diagonal (from ~He$_5$V$_5$ to He$_{10}$V$_9$). According to our thermodynamic binding energy model, both the He- and V-binding energies increase as the cluster size increases at a fixed He/V ratio of ~1. This quickly results in a fast growth of the larger clusters while the small clusters (below He$_5$V$_5$) continue to dissociate. Thus this process can be called a helium-vacancy coordinated Ostwald ripening. As can be seen in Fig. 4, the front of the composition line grows to about He$_{100}$V$_{100}$ by 750 °C after the He$_3$V$_2$ completely dissociates, and further to He$_{400}$V$_{400}$ by 900 °C after most of the remaining HeV clusters dissolve. During this He–V coordinated Ostwald ripening, both the very small clusters such as He$_3$V$_2$ and HeV as well as larger clusters throughout the growing composition line contribute to the He desorption flux to the free surface. The ripened clusters which do not have sufficient time or thermal energy to be fully desorbed before the BCC ↔ FCC phase transformation will be carried over to higher temperatures in the FCC regime.

This may provide an explanation for the source of the much stronger release signals in the FCC regime observed for the higher fluence specimens (see Fig. 1). Due to the continuous loss of He, the growth of the ripened larger clusters may slow or completely stop at some temperatures within the FCC regime, which of course depends on the remaining concentrations of the ripened clusters and the energetics and kinetics of He in FCC iron. Since the energetics and kinetics of He in FCC iron have not been well studied, our current modeling is limited only to the BCC regime.

5. Conclusions

A newly developed, parallel computer code for modeling the spatially-dependent cluster dynamics of He, vacancy and interstitial clusters has been used to predict the thermal desorption of single crystal iron implanted with ^{4}He$^+$ ions at 5 or 10 keV energies to intermediate and high fluences of 10^{18} or 10^{19} He/m^2. The model takes as input *ab* initio data for the migration energies of He, SIA and di-SIA, *ab* initio extrapolated binding energies for V$_m$ and I$_n$ clusters, and thermodynamically calculated binding energies for He$_x$V$_y$ clusters. The present results demonstrate that a reasonably consistent prediction of the experimentally observed He desorption can be obtained through a relatively small amount of parameter optimization. In particular, the model reasonably well

reproduces the experimentally observed number of major desorption groups and the temperatures of the desorption peaks. However, further improvement is required for better reproduction of peak intensities and the splitting of a strong peak centering around 800 °C. Analysis of cluster distribution in the phase space at varying temperatures discloses an evolution sequence closely related to the He/V ratio. At low temperatures, clusters with either high or low He/V ratios evolve towards an intermediate ratio (from about 1 to ∼1.6), with the 10^{18} He/m^2 specimens displaying a unique vacancy-dominated Ostwald ripening phenomenon. At high temperatures (above 550 °C), the clusters in the lower fluence (10^{18} He/m^2) implanted specimens simply shrink along a line in the phase space corresponding to a He/V ratio of ∼1, while the clusters in the higher fluence (10^{19} He/m^2) implanted specimens experience significant and coordinated helium-vacancy Ostwald ripening. The sources of desorbed He are discussed for all the stages which are closely tied with the overall cluster evolution dynamics. The ripened large He–V clusters may explain the source of the much stronger release signals in the FCC regime observed for the higher fluence specimens.

Acknowledgment

References

[1] H. Ullmaier, Nucl. Fusion 24 (1984) 1039.
[2] L.K. Mansur, M.L. Grossbeck, J. Nucl. Mater. 155 (1988) 130.
[3] L.K. Mansur, W.A. Coghlan, J. Nucl. Mater. 119 (1983) 1.
[4] K.C. Russell, Acta Metall. 26 (1978) 1615.
[5] R.E. Stoller, G.R. Odette, J. Nucl. Mater. 131 (1985) 118.
[6] L.K. Mansur, E.H. Lee, P.J. Maziasz, A.P. Rowcliffe, J. Nucl. Mater. 141–143 (1986) 633.
[7] H. Trinkaus, Radiat. Eff. Defects Solids 78 (1983) 189.
[8] K.C. Russell, Acta Metall. 20 (1972) 899.
[9] K. Morishita, R. Sugano, B.D. Wirth, T.D. de la Rubia, Nucl. Instrum. Methods Phys. Res. B 202 (2003) 76.
[10] B.D. Wirth et al., J. Nucl. Mater. 329 (2004) 103.
[11] C.C. Fu, F. Willaime, Phys. Rev. B 72 (2005) 064117.
[12] T. Seletskaia, Y.N. Osetsky, R.E. Stoller, G.M. Stocks, J. Nucl. Mater. 351 (2006) 109.
[13] H.L. Heinisch, F. Gao, R.J. Kurtz, E.A. Le, J. Nucl. Mater. 351 (2006) 141.
[14] C.J. Ortiz, M.J. Caturla, C.C. Fu, F. Willaime, Phys. Rev. B 75 (2007) 100102.
[15] K. Ono et al., J. Nucl. Mater. 329–333 (2004) 933.
[16] M.B. Lewis, K. Farrell, Nucl. Instrum. Methods Phys. Res. B 16 (1986) 163.
[17] T. Ishizaki, Q. Xu, T. Yoshiie, S. Nagata, T. Troev, J. Nucl. Mater. 307 (2002) 961.
[18] R. Sugano, K. Morishita, A. Kimura, Fusion Sci. Technol. 44 (2003) 446.
[19] R. Vassen, H. Trinkaus, P. Jung, Phys. Rev. B 44 (1991) 4206.
[20] D.H. Xu, B.D. Wirth, J. Nucl. Mater. 386 (2009) 395.
[21] D.H. Xu, B.D. Wirth, Fusion Sci. Technol. 56 (2009) 1064.
[22] C.J. Ortiz et al., J. Appl. Phys. 96 (2004) 4866.
[23] S.I. Golubov, A.M. Ovcharenko, A.V. Barashev, B.N. Singh, Phil. Mag. A 81 (2001) 643.
[24] J.F. Ziegler, J.P. Biersack, U. Littmark, The Stopping and Range of Ions in Matter, Pergamon, New York, 1984.
[25] C.C. Fu et al., Nat. Mater. 4 (2005) 68.
[26] C.J. Ortiz, M.J. Caturla, C.C. Fu, F. Willaime, Phys. Rev. B 80 (2009) 134109.